

## RESEARCH ARTICLE

10.1029/2017JB014936

## Key Points:

- The midcrust throughout the Central Andes is characterized by positive radial anisotropy resulting from ductile crustal flow
- Ductile crustal flow in the Central Andes extends to at least 40 km depth and may extend deeper
- We observe very strong positive radial anisotropy in the APVC likely due to a horizontally layered magmatic storage system

## Supporting Information:

- Supporting Information S1

## Correspondence to:

C. Lynner,  
c1l44@email.arizona.edu

## Citation:

Lynner, C., Beck, S. L., Zandt, G., Porritt, R. W., Lin, F.-C., & Eilon, Z. C. (2018). Midcrustal deformation in the Central Andes constrained by radial anisotropy. *Journal of Geophysical Research: Solid Earth*, 123. <https://doi.org/10.1029/2017JB014936>

Received 30 AUG 2017

Accepted 28 APR 2018

Accepted article online 5 MAY 2018

## Midcrustal Deformation in the Central Andes Constrained by Radial Anisotropy

Colton Lynner<sup>1</sup> , Susan L. Beck<sup>1</sup> , George Zandt<sup>1</sup>, Robert W. Porritt<sup>2</sup> , Fan-Chi Lin<sup>3</sup> , and Zachary C. Eilon<sup>4</sup> 

<sup>1</sup>Department of Geosciences, University of Arizona, Tucson, AZ, USA, <sup>2</sup>Institute for Geophysics, University of Texas, Austin, TX, USA, <sup>3</sup>Department of Geology and Geophysics, University of Utah, Salt Lake City, UT, USA, <sup>4</sup>Department of Earth Science, University of California, Santa Barbara, Santa Barbara, CA, USA

**Abstract** The Central Andes are characterized by one of the largest orogenic plateaus worldwide. As a result, they are home to some of the thickest continental crust observed today (up to ~75-km thick). Understanding the response of the crust to such overthickening provides insights into the ductile behavior of the midcrust and lower crust. One of the best tools for examining crustal-scale features is ambient noise tomography, which takes advantage of the ambient noise wavefield to sample crustal depths in great detail. We extract Love and Rayleigh wave phase velocities from ambient noise data to invert for  $V_{sh}$ ,  $V_{sv}$ , and radial anisotropy throughout the Central Andes. We capture detailed crustal structure, including pronounced along-strike isotropic velocity heterogeneity and substantial (up to 10%) radial anisotropy that varies with depth. This crustal anisotropy may have several origins, but throughout the majority of the Central Andes, particularly beneath the Altiplano, we interpret radial anisotropy as the result of mineral alignment due to ductile crustal deformation. Only in the strongly volcanic Altiplano-Puna Volcanic Complex is radial anisotropy likely caused by magmatic intrusions.

### 1. Introduction

The Central Andes, spanning parts of Peru, Bolivia, Argentina, and Chile, were formed as an orogenic mountain belt due to the subduction of the Nazca oceanic plate beneath continental South America (e.g., Allmendinger et al., 1997; Isacks, 1988). Subduction along the South American plate boundary varies laterally, with regions of normal (e.g., southern Peru and northern Chile) and flat-slab (e.g., central Peru and southern Chile) subduction. These variations in slab dip angle have led to different styles of crustal deformation in the overriding South American plate (e.g., Cahill & Isacks, 1992; Kley et al., 1999). This is exemplified by the presence of the Central Andean Plateau (CAP) and the Bolivian Orocline, which were caused by extreme crustal shortening (see reviews by Garzzone et al., 2017; Gotberg et al., 2010).

The CAP, composed of the Altiplano and Puna plateaus, lies between two regions of flat-slab subduction and is bounded by the Eastern and Western Cordilleras (Figure 1). The CAP represents the second largest orogenic plateau on the planet with an average elevation  $>3$  km spanning an area  $\sim 1,800$  km long by  $\sim 400$  km wide. In addition to high topography, the CAP is characterized by crustal thicknesses of up to  $\sim 75$  km (e.g., Assumpção et al., 2013; Beck et al., 1996; Heit et al., 2014; Mamani et al., 2010; Ryan et al., 2016; Yuan et al., 2000). An important factor in the formation of the CAP is the westward migration of the South American plate boundary resulting in substantial crustal shortening (potentially greater than 300 km; Garzzone et al., 2017). Significant shortening along the margin, however, is not ubiquitous. It is locally focused near the Bolivian Orocline, with less shortening of the overriding plate to the north and south of the CAP. There has been a concerted effort to understand the response of the midcrust and lower crust to large crustal thicknesses resulting from tectonic shortening (e.g., Beaumont et al., 2001, 2006; Chen et al., 2016; Cheng et al., 2013; Guo et al., 2012; Guo et al., 2016; Huang et al., 2010; Ling et al., 2017; Luo et al., 2013; Moschetti et al., 2010; Ojo et al., 2017; Pawlak et al., 2012; Royden et al., 1997; Shapiro et al., 2004; Shirzad et al., 2017; Shirzad & Shomali, 2014; Xie et al., 2013). In the Andes, numerous studies have suggested north-south crustal flow away from the regions with highest estimated shortening, near the Bolivian Orocline, to regions with less shortening (Eichelberger et al., 2015; Gerbault et al., 2005; Hindle et al., 2005; Husson & Sempere, 2003; Kley & Monaldi, 1998; McQuarrie et al., 2005; Oncken et al., 2006; Ouimet & Cook, 2010; Schepers et al., 2017; Yang et al., 2003).

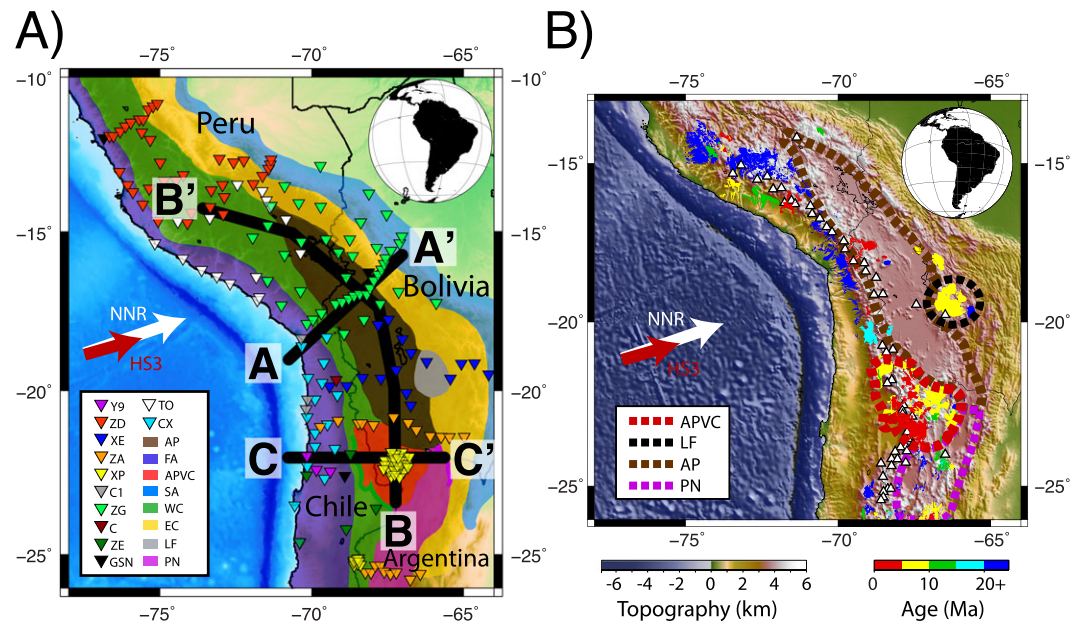


**Figure 1.** (a) Morphotectonic provinces of the Central Andes (after Tassara, 2005; Turienzo et al., 2012; colored by region: AP = Altiplano; FA = Forearc; APVC = Altiplano-Puna Volcanic Complex; SA = Sub-Andes; WC = Western Cordillera; EC = Eastern Cordillera; LF = Los Frailes Volcanic Complex; PN = Puna Plateau), and stations (colored by network) used in this study; see legend for both. Transects A-A', B-B', and C'-C correspond to the cross sections shown in Figures 7, 8, and 9, respectively. The convergent motion of the Nazca plate in no-net-rotation (NNR; DeMets et al., 2010) and hotspot (HS3-Nuvel 1A; Gripp & Gordon, 2002) reference frames are shown by the white and red arrows, respectively. (b) Ignimbrite deposits in our study region. The APVC, AP, LF, and PN regions are outlined. Active Holocene volcanoes are shown as white triangles.

Most studies aimed at midcrustal to lower crustal flow have focused on the Tibetan plateau. The Tibetan plateau is characterized by crustal thicknesses similar to those beneath the CAP (70–80-km thick; Fielding et al., 1994) making it an excellent analog for the Central Andes. Extensive geophysical (e.g., Chen et al., 2016; Guo et al., 2012; Huang et al., 2010; Shapiro et al., 2004; Shen et al., 2005; Xie et al., 2013) and geological (e.g., Clark & Royden, 2000; Wang & Burchfiel, 2000) studies across the Tibetan plateau have aimed to understand the response of the crust to the high plateau topography. These studies all suggest the presence of ductile deformation of the midcrust to lower crust. What remains unclear is whether the crustal behavior of the Tibetan plateau is unique or is broadly applicable to other orogenic systems with similarly thick crust, such as the CAP.

Crustal flow beneath the Tibetan plateau manifests in distinct surface and geophysical observables such as shallow topographic gradients where crustal material is escaping (e.g., Clark & Royden, 2000; Royden et al., 1997) and the development of strong positive radial anisotropy in the deforming crust (e.g., Chen et al., 2016; Guo et al., 2012; Huang et al., 2010; Shapiro et al., 2004; Xie et al., 2013). There are no readily apparent surface structures associated with the CAP indicating ductile crustal deformation except the relatively flat topography of the Altiplano. With the amount of shortening experienced by the South American crust, however, there must be a mechanism for the escape of crustal material (e.g., Garzzone et al., 2017). Deformational events in the South American crust, therefore, can best be inferred through observations of seismic anisotropy.

Radial anisotropy refers to cases where (relative to the propagation direction of surface waves) vertically ( $V_{sv}$ ) and horizontally ( $V_{sh}$ ) polarized shear waves have different velocities (e.g., Bensen et al., 2009; Moschetti et al., 2010). Radial anisotropy develops in the crust through the alignment of anisotropic minerals via deformation, aligned cracks and structures, and/or layered structures (Figure 2; e.g., Crampin, 1981, 1984, 1987; Crampin & Lovell, 1991; Leary et al., 1990; Mainprice & Nicolas, 1989; Shapiro et al., 2004; Meissner et al., 2006; Moschetti et al., 2010). The most important radially anisotropic minerals in the crust are micas, which are strongly anisotropic and when deformed will rotate within the deformation geometry such that the seismically slow orientation aligns orthogonally to the orientation of deformation (e.g., Lloyd et al., 2009; Tatham et al., 2008).

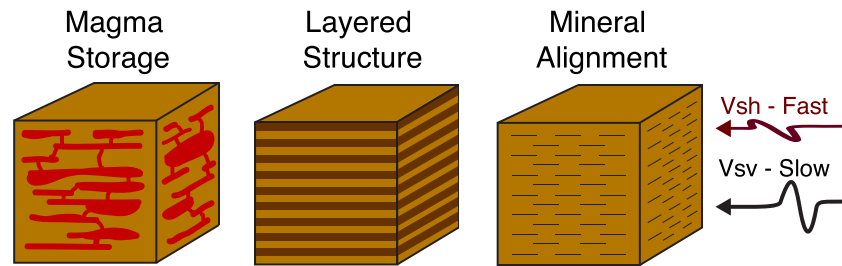


**Figure 2.** Cartoon of likely scenarios leading to positive radial anisotropy ( $V_{sh} > V_{sv}$ ) in the crust.

In regions of substantial melt, radial anisotropy can develop due to the horizontal (or vertical) alignment of melt lenses or storage structures (e.g., Kawakatsu et al., 2009; Takeuchi et al., 1968). In such cases, the elastic properties of the melt and the surrounding material are sufficiently different to result in a shape-preferred radial anisotropy where the seismically slow orientation aligns orthogonally to the alignment of the melt pockets (which themselves are aligned perpendicular to  $\sigma_3$ ). Gaining constraints on radial anisotropy from crustal shear velocities, therefore, allows us to make inferences about structures and/or deformation in the middle to lower crust.

Ambient noise tomography (ANT) can be used to extract empirical Green's functions (EGFs) of both Rayleigh and Love waves to invert for shear velocity (e.g., Bensen et al., 2008; Lin et al., 2008). Ambient noise data provides constraints at short periods allowing crustal-scale resolution. Inverting both Rayleigh and Love phase velocities for shear velocity gives us constraints on  $V_{sv}$ ,  $V_{shr}$  and radial anisotropy (RA; here defined as  $RA = ((V_{sh}/V_{sv})-1)\times 100$ ). Here we present ANT results from Love and Rayleigh wave EGFs across the Central Andes. We invert for  $V_{shr}$ ,  $V_{sv}$ , and radial anisotropy throughout our study area (Figure 1).

## 2. Background

### 2.1. Geologic Setting

The Central Andes are composed of several major morphotectonic provinces including: the fore-arc region (FA), the Eastern Cordillera (EC), the Western Cordillera (WC), the Altiplano plateau (AP), the Puna plateau (PN), the Sub-Andes (SA), the Los Frailes Volcanic Complex (LF), and the Altiplano-Puna Volcanic Complex (APVC; Figure 1). The entire region owes its formation to the convergence of the Nazca and South American plates at a rate of  $\sim 60$ – $80$  mm/year (e.g., Allmendinger et al., 1997; Isacks, 1988; Kendrick et al., 2001; Lamb & Hoke, 1997; Lynner et al., 2017). In the CAP region, a significant portion of the convergence has been accommodated by deformation of the western margin of the overriding South American plate ( $\sim 15$  mm/year; Norabuena et al., 1998). The increased shortening of the crust has led to the formation of the Bolivian Orocline and to the high topography and associated large crustal thicknesses (in excess of  $\sim 70$  km; Tassara & Echaurren, 2012) of the Altiplano and Puna plateaus.

The forearc region of the Central Andes runs from the trench to the Western Cordillera, which represents the modern active volcanic arc ( $\sim 150$ – $200$  km inland from the coast). The width of the Western Cordillera is highly variable along strike; narrow near the Bolivian Orocline, and wide north and south of the Altiplano. The Eastern Cordillera represents an inactive fold and thrust belt with some Triassic and Miocene intrusions. The Eastern Cordillera experienced significant crustal shortening before the deformation front moved eastward into the Sub-Andes roughly 10 Ma (Echavarría et al., 2003; Gubbels et al., 1993; Horton & DeCelles, 1997). Between the Eastern and Western Cordilleras lie the Altiplano and Puna plateaus (comprising the CAP). Both exhibit high topography ( $>3$  km) and large crustal thicknesses (up to  $\sim 75$  km; e.g., Assumpção et al., 2013; Beck et al., 1996; Mamani et al., 2010; Ryan et al., 2016). The Puna is  $\sim 1$  km higher, has more surface relief, and more widespread volcanism than the Altiplano (Figure 1). Today, both plateaus are experiencing little to no deformation. While much remains uncertain about the deformation histories and fault geometries at depth beneath the Altiplano and Puna plateaus, crustal thicknesses beneath the CAP suggest that significant shortening must have occurred.

Between the Altiplano and Puna plateaus (at the confluence of the Bolivian, Chilean, and Argentinean borders) lies the APVC, which sits at an average elevation higher than 4 km (Figure 1). The APVC is characterized by dominantly calc-alkaline ignimbrites (e.g., De Silva, 1989; Salisbury et al., 2010). Material associated with the volcanic complex is remarkably chemically homogeneous while being distributed over an area of  $\sim 70,000$  km<sup>2</sup> (De Silva et al., 2006). Eruptions associated with the APVC began  $\sim 11$  Ma, peaked  $\sim 4$  Ma, and have subsequently subsided to background levels (Salisbury et al., 2010). Magmas in the region are derived from both mantle and crustal sources suggesting mixing and residence in the crust (Kay et al., 2010; Schilling et al., 2006). Seismic work has suggested the primary magma body of the APVC is centered at  $\sim 15$ -km depth (Chmielowski et al., 1999; Ward et al., 2013; Zandt et al., 2003) and represents a very large magma body with a volume of  $>500,000$  km<sup>3</sup> (Ward et al., 2014).

## 2.2. Radial Anisotropy

Radial seismic anisotropy refers to cases where horizontally ( $V_{sh}$ ) and vertically ( $V_{sv}$ ) polarized shear waves (relative to propagation direction) travel at different velocities (e.g., Bensen et al., 2009; Moschetti et al., 2010). In the crust, positive radial anisotropy ( $V_{sh} > V_{sv}$ ) is typically interpreted as reflecting horizontally aligned structures (cracks or layers) or the horizontal alignment of crystalline axes of anisotropic minerals, such as micas, while negative radial anisotropy ( $V_{sv} > V_{sh}$ ) is generally interpreted as vertical structures or mineral alignment (e.g., Crampin, 1981, 1984, 1987; Crampin & Lovell, 1991; Leary et al., 1990; Mainprice & Nicolas, 1989; Meissner et al., 2006; Shapiro et al., 2004). Anisotropy is seismically observable when the alignment of structures or mineral axes is pervasive and has a broadly organized orientation (e.g., Moschetti et al., 2010). We measure radial anisotropy in the crust through the determination of shear velocities from Rayleigh (sensitive to  $V_{sv}$ ) and Love (sensitive to  $V_{sh}$ ) waves (e.g., Bensen et al., 2009; Chen et al., 2016; Cheng et al., 2013; Guo et al., 2012, 2016; Huang et al., 2010; Ling et al., 2017; Luo et al., 2013; Moschetti et al., 2010; Ojo et al., 2017; Pawlak et al., 2012; Shapiro et al., 2004; Shirzad et al., 2017; Shirzad & Shomali, 2014; Xie et al., 2013). By inverting both phases, we constrain radial anisotropy at depths with overlapping sensitivity.

Radial seismic anisotropy in the crust has several possible causes, such as the shape-preferred orientation (SPO) of melt lenses, faults, and/or other structures or the crystallographic-preferred orientation (CPO) of anisotropic minerals (Figure 2). SPO anisotropy arises when layers with different elastic properties become aligned (see Karato, 2012). This may be due to sedimentary layering, structural features such as faults or folds, or magmatic intrusions such as dykes and/or sills or melt lenses. SPO anisotropy derived from magmatic sources is typically stronger than other CPO anisotropy as the elastic contrast between crustal material and melts is very high (e.g., Holtzman et al., 2003; Karato, 2012). Since melts do not support shear stresses, melt-related anisotropy impacts  $V_{sh}$  and  $V_{sv}$  very differently. In the case of horizontally aligned melt lenses or sills,  $V_{sv}$  will be reduced more severely than  $V_{sh}$  (e.g., Kawakatsu et al., 2009; Takeuchi et al., 1968).

Radial anisotropy in the crust is typically interpreted, however, as deformation-induced CPO of anisotropic minerals, not SPO of structures (e.g., Moschetti et al., 2010). While volumetrically small in the crust, micas are the most important anisotropic minerals (e.g., Lloyd et al., 2009; Tatham et al., 2008). Quartz and other volumetrically dominant crustal minerals are isotropic to weakly anisotropic or do not deform in such a way as to produce strong radial anisotropy (Lloyd et al., 2009; Mahan, 2006; Nishizawa & Yoshino, 2001; Ward et al., 2012). When deformed, micas tend to align such that the seismically slow axis orients orthogonally to the deformation direction. This results in fast seismic velocities in the plane that parallels the orientation of flow. In the case of horizontal deformation in the crust, mica alignment would produce fast seismic velocities in the horizontal plane, resulting in positive radial anisotropy ( $V_{sh} > V_{sv}$ ) for horizontally propagating surface waves.

## 3. Data and Methods

The cross correlation of ambient noise data between seismic stations can be used to calculate EGFs of Rayleigh and Love waves traveling between the sites (e.g., Bensen et al., 2008; Lin et al., 2008). Extracting surface wave dispersion relationships from noise-generated EGFs and inverting for phase velocities is referred to as ambient noise tomography. ANT is a useful tool for interrogating crustal-scale shear velocities and anisotropic structures because it is sensitive to shorter periods (between 8 s and 40 s) that travel predominantly in the crust (Figure S1 in the supporting information). Because the ambient noise wavefield acts upon every

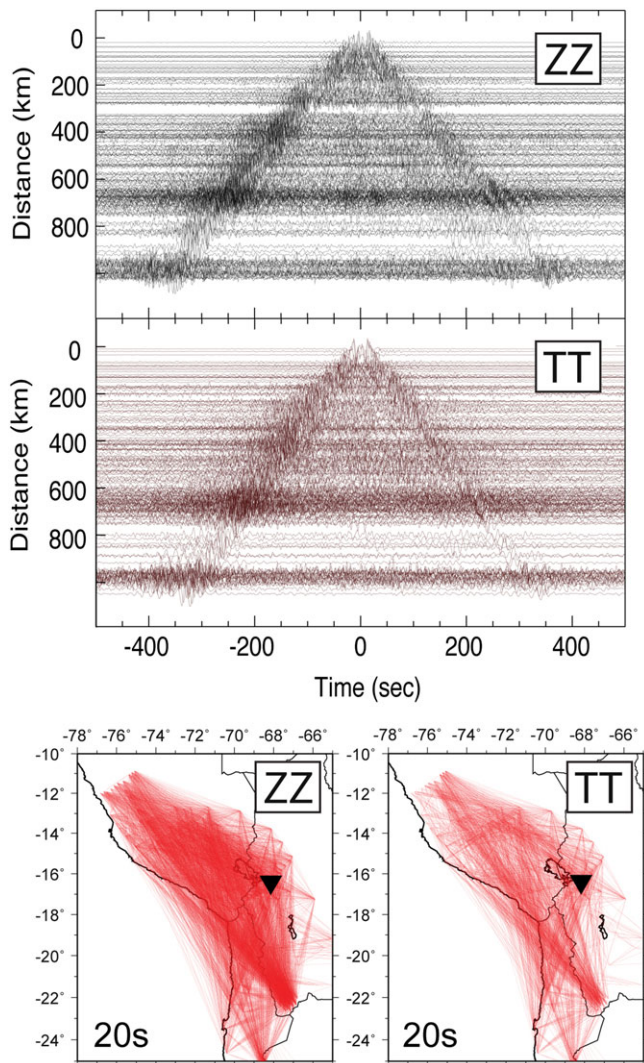


**Figure 3.** (top) Initial ZZ and TT component cross-correlation EGFs (filtered between 5 s and 150 s) between long-running station LPAZ in Bolivia and all contemporaneously operating stations. (bottom) Interstation paths for ZZ and TT cross-correlations at 20 s that pass the quality control criteria described in the text. Station LPAZ is shown as an inverted black triangle.

contemporaneously operating seismic station, we can treat each station as both a virtual source and a receiver resulting in very dense ray coverage in the Central Andes (Figures 3 and S2).

We use data from all running seismic stations operating in our study area between 1994 and 2016 (Figure 1). Our data set includes data from 14 networks and 206 seismic stations. We follow the methodologies of Bensen et al. (2008) and Lin et al. (2008). We segment vertical, east, and north component waveforms into daylong intervals. The waveforms are initially downsampled to one sample per second, demeaned, detrended, corrected for station response, tapered, and whitened. A running-absolute-mean temporal normalization is then applied to each daylong segment to remove earthquake-generated sources. This ensures that EGFs carry only noise-generated Rayleigh and Love wave signals. The segments are then cross-correlated for all potential station pairs and are stacked to produce EGFs (Figure 3). For each station pair, nine cross correlations are produced. All components at both stations are cross-correlated (Z-vertical, N-north, E-east; ZZ, ZN, ZE, EE, EN, EZ, NN, NE, and NZ). We then rotate the horizontal component cross correlations into interstation orientations producing radial and transverse component cross correlations. Both vertical-vertical (ZZ) and radial-radial (RR) component EGFs provide constraints on Rayleigh wave velocities, and the transverse-transverse (TT) component EGFs reflect primarily Love waves with only a minute sensitivity to Rayleigh waves, which we consider here to be negligible.

We employ traditional frequency-time analysis (e.g., Levshin et al., 1992) to the EGFs and measure Rayleigh and Love wave phase velocities for the appropriate cross correlations. We calculate phase velocities at periods between 8 and 40 s. We retain dispersion values from EGFs with signal-to-noise ratios (SNRs) greater than 10, and we reject those resulting from station pairs with interstation path lengths less than two wavelengths in order to avoid the overlapping of surface wave energy with precursory arrivals and to satisfy the far-field approximation. Luo et al. (2015) demonstrated that dispersion results from interstation distances greater than one wavelength are reliable, and many subsequent studies have used interstation path lengths less than three wavelengths to great success (e.g., Jiang et al., 2016; Lynner & Porritt, 2017; Ojo et al., 2017; Porritt et al., 2016). From the calculated ZZ, RR, and TT phase velocities, we invert for regional phase velocity maps for each period on a  $0.1^\circ$  by  $0.1^\circ$  grid following Barmin et al. (2001) as shown in Figures 4 and S3–S5

(using regularization parameters  $\alpha = 600$  and  $\beta = 200$  with a correlation length of  $\gamma = 200$ ; see Barmin et al., 2001 for an in depth description of the inversion parameters). We tested several combinations of inversion parameters and found these to produce the best results. We then separately invert for shear velocities ( $V_{sv}$  from ZZ components and  $V_{sh}$  from TT components) and radial anisotropy using the results of the phase velocity inversions (Herrmann, 2013). Because both RR and ZZ component cross correlations provide constraints on Rayleigh wave phase velocities, we use the ZZ component-derived phase velocities for final reporting of  $V_{sv}$  and radial anisotropy. The ZZ cross correlations are generally higher amplitude than RR and thus have better SNRs. Using ZZ over RR cross correlations results in a greater number of interstation paths that pass the quality control steps above (Figure S2).

Shear velocity inversions (Herrmann, 2013) are parameterized using 2-km-thick layers in the upper 50 km of model, 5-km-thick layers from 50 km to 100 km depth, and 10-km-thick layers below 100 km. We invert for  $V_{sh}$  and  $V_{sv}$  separately using identical starting models and inversion parameters. Our initial model is set to AK135 (Kennett et al., 1995) below 100 km and 4.5 km/s in the upper 100 km without an artificial jump at the Moho to avoid low velocity artifacts (e.g., Lynner & Porritt, 2017). We tested several starting models with a spatially

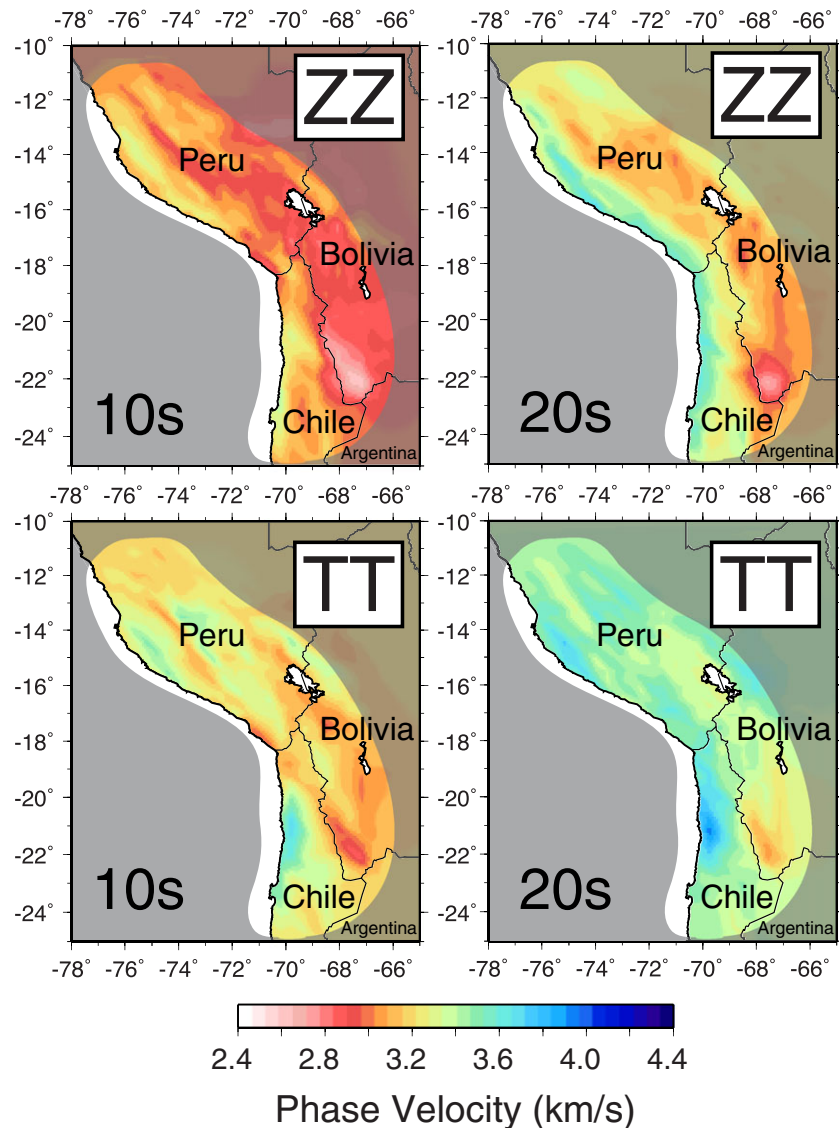


**Figure 4.** Phase velocity maps inverted from ZZ (top) and TT (bottom) component cross correlations at 10-s (left) and 20-s (right) periods. The regions outside of which these models have resolution are shaded.

varying velocity jump at the Moho and found that the different starting models resulted in only minor deviations. We have chosen, therefore, to use the starting model with the least amount of initial complexity. We correct for topography using the ETOPO global topography model (Amante & Eakins, 2009) to avoid artifacts from the high CAP elevations. Due to the different sensitivities of Rayleigh and Love waves, we only have sensitivity of  $V_{sh}$  (and, therefore, also radial anisotropy) to depths of  $\sim 40$  km, while the  $V_{sv}$  inversion is sensitive between  $\sim 4$ -km and  $\sim 50$ -km depth (Figures S1, S6, and S7). Our models have different resolutions at different depths owing to differences in ray coverage of ZZ and TT cross correlations (Figure S2) and different sensitivity kernels (Figure S1). We therefore only interpret features resolvable by the least well-resolved phase. For the majority of this study, this corresponds to features in the midcrust with lateral dimensions of  $\sim 100$  km<sup>2</sup> and  $\sim 4$  km in depth. The region of maximum resolution lies between  $\sim 10$ -km and  $\sim 25$ -km depth, with decreasing resolution both above and below.

The strength of ANT lies in the ability to sample crustal velocity structure from both Love and Rayleigh wave phase velocities without the need for earthquake-generated sources (e.g., Lin et al., 2008). Best practices in ANT are still being developed due to the relatively new emergence of the technique. The underlying

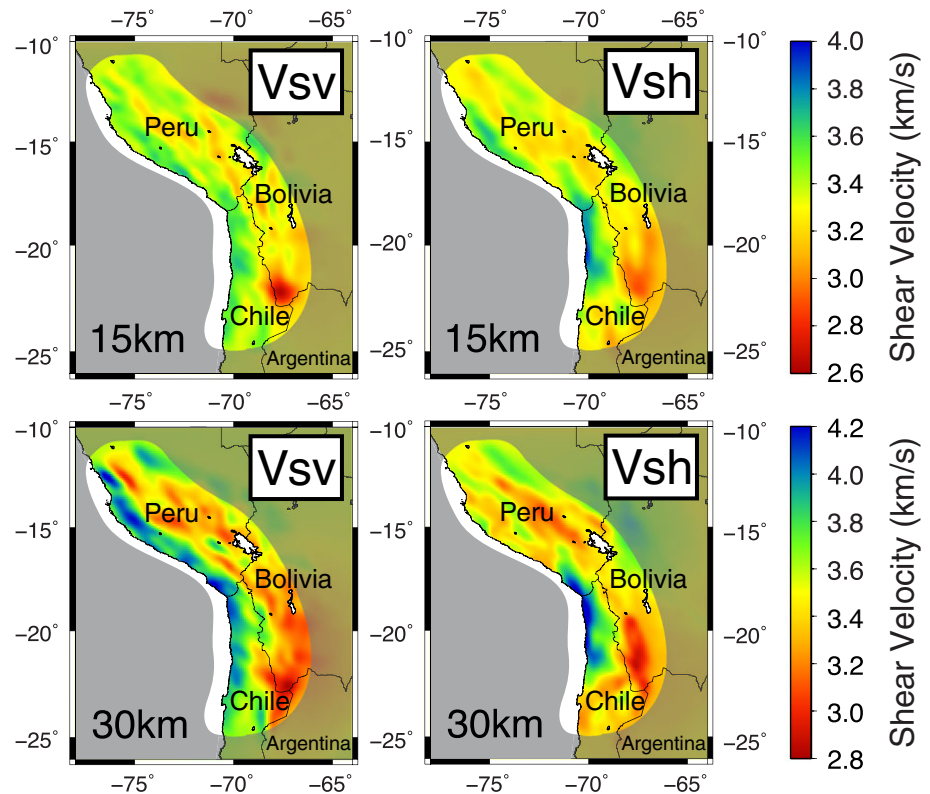


**Figure 5.** Shear velocity maps of our  $V_{sv}$  (left) and  $V_{sh}$  (right) models at depths of 15 km (top) and 30 km (bottom). Regions outside of our model resolution are obscured.

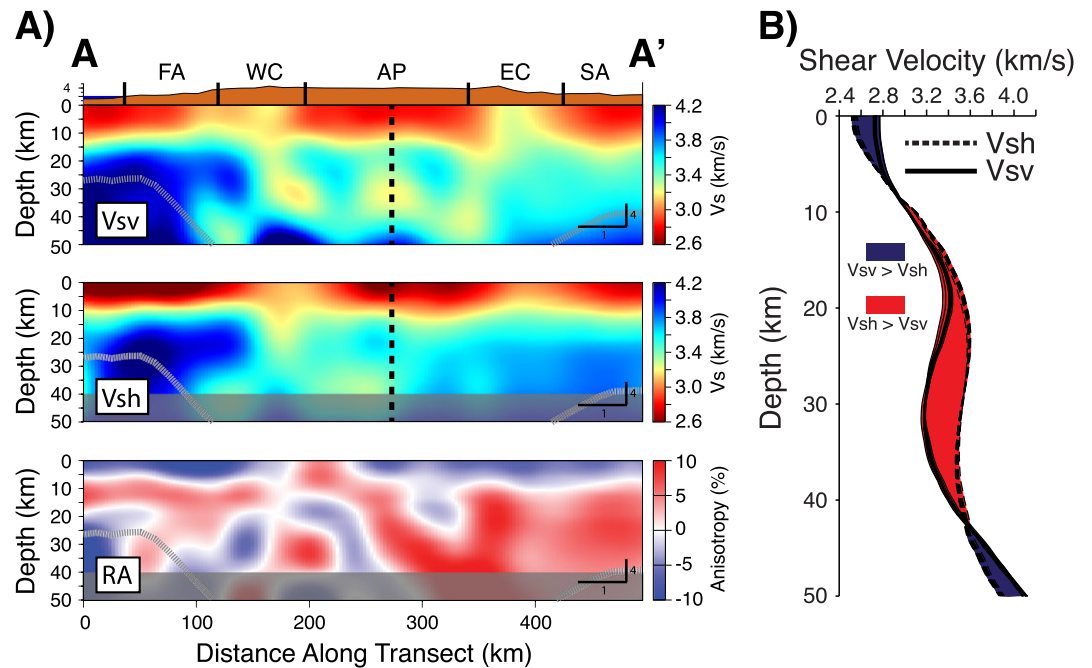


**Figure 6.** (a) Cross sections of  $V_{sv}$ ,  $V_{sh}$ , and radial anisotropy along the transect A-A' shown in Figure 1. Morphotectonic provinces following Figure 1 are indicated at the top. Dashed black lines denote the depth profile shown in (b). Gray dashed lines denote the Moho from Crust1.0 (Hayes et al., 2012). Depths below our resolution are obscured. (b) Depth profiles of  $V_{sh}$  (dashed lines) and  $V_{sv}$  (solid lines) from 10 of our bootstrap runs. Regions of positive and negative radial anisotropy are highlighted by red and blue, respectively.

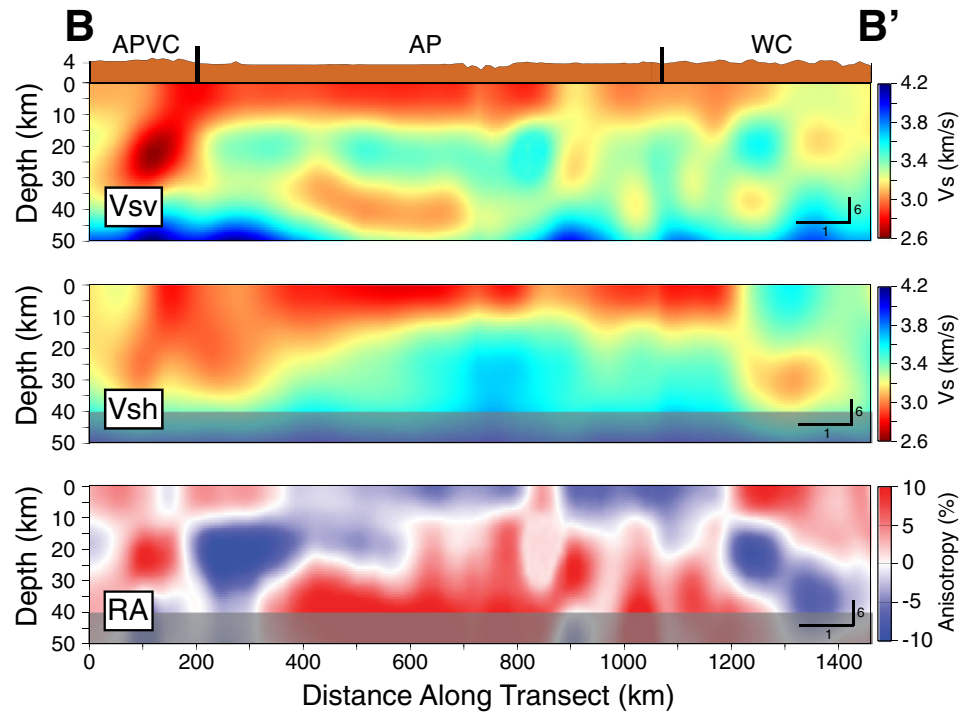


**Figure 7.** Cross section along transect B-B' that runs along the length of the CAP roughly following the South American plate boundary. Depth velocity profiles for the CAP and APVC can be seen in Figures 6 and 8. Figure conventions are the same as in Figure 6.

theory of ANT rests upon the assumption that ambient noise sources are equally distributed with back azimuth and in amplitude. Noise sources such as wave-generated and storm-generated noise are, however, typically asymmetric in nature. Deviations such as these can introduce artifacts into the cross correlations (e.g., Fichtner, 2014, 2015). These artifacts are greatly reduced when taking cross correlations over periods of greater than 1 year and averaging both sides of the EGFs (e.g., Lin et al., 2008; Porritt et al., 2011), which are both done in this study.

#### 4. Results

$V_{sh}$  and  $V_{sv}$  shear velocity inversions at depths of 15 km and 30 km are shown in Figure 5. Regional Rayleigh and Love wave phase velocity inversions can be found in Figures 4, S3, and S4.  $V_{sv}$ ,  $V_{sh}$ , and radial anisotropy cross sections through the central CAP, along the Altiplano, and through the APVC can be seen in Figures 6, 7, and 8, respectively. Apparent in both the  $V_{sh}$  and  $V_{sv}$  shear velocity models are fast fore-arc velocities, a slow APVC anomaly, and relatively consistent velocities beneath the Altiplano (Figure 5). This is in strong agreement with previous ANT work in the region (Ward et al., 2013).

From the  $V_{sv}$  and  $V_{sh}$  shear velocity models, it is readily apparent that radial anisotropy persists throughout the Central Andean crust. To confirm that this feature is not an artifact of the inversion, we calculated forward models to demonstrate that radial anisotropy is required to explain our observed Rayleigh and Love wave dispersion measurements (Figure 9) and that our inversion scheme adequately captures radial anisotropy in the crust (Figure 10). We calculated dispersion relationships for Love and Rayleigh waves for anisotropic and isotropic models in both the APVC and Altiplano and find that for both regions anisotropy is required by the data (Figure 9). Figure 10 shows that our inversion scheme successfully inverts for crustal radial anisotropy, albeit underestimating the magnitude of anisotropy.

Beneath the Altiplano, positive radial anisotropy is observed between shallow depths (10 km to 15 km) and the bottom of our model in both cross sections A-A' (Figure 6; which crosses the Altiplano) and B-B' (Figure 7; which runs along the length of the CAP). The variations in shear velocity with depth beneath the Altiplano (Figure 6b) follow similar trends in both  $V_{sv}$  and  $V_{sh}$  models, with  $V_{sv}$  showing slightly slower velocities

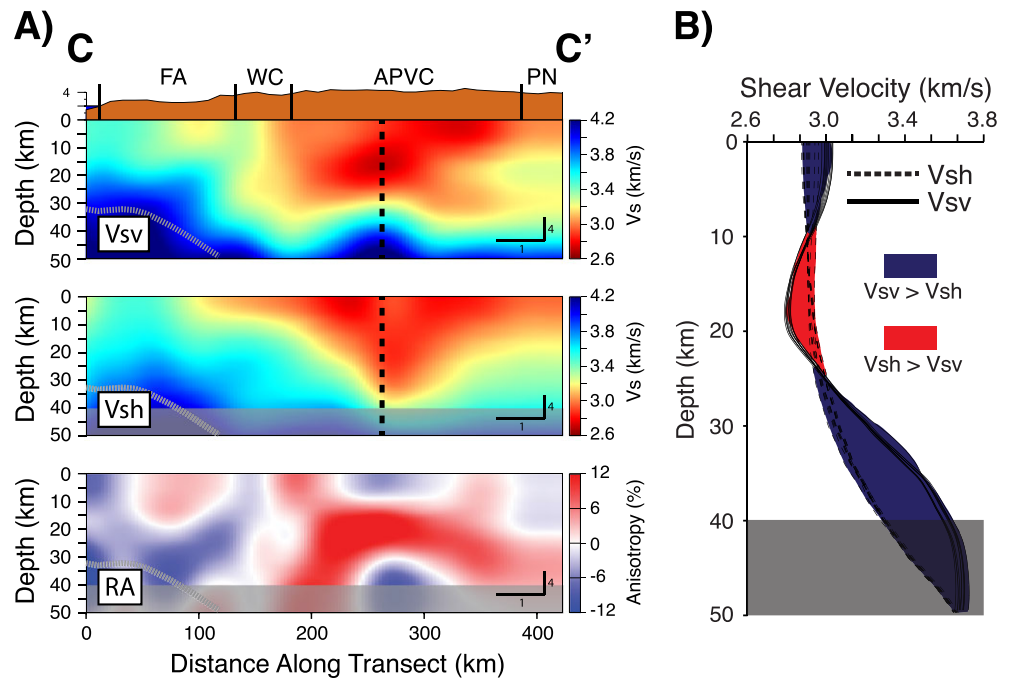


**Figure 8.** (a) Cross section along transect C-C' that samples the APVC. (b) Depth profiles of  $V_{sh}$  and  $V_{sv}$ . Figure conventions are the same as in Figure 6.

throughout. To both the north and south of the Altiplano-related positive radial anisotropy lie areas of negative radial anisotropy (Figure 7). The southern region of negative radial anisotropy separates the Altiplano-related from the APVC-related positive anisotropy. Beneath the APVC, very strong ( $>12\%$ ) radial anisotropy is observed at midcrustal depths. Unlike in the Altiplano, the positive radial anisotropy associated with the APVC arises from the preferential reduction of  $V_{sv}$  relative to  $V_{sh}$ . This is apparent in the diverging trends in shear velocity with depth through the slow velocity anomaly (Figure 8b). Both above and below the APVC region of positive radial anisotropy are regions of negative radial anisotropy.

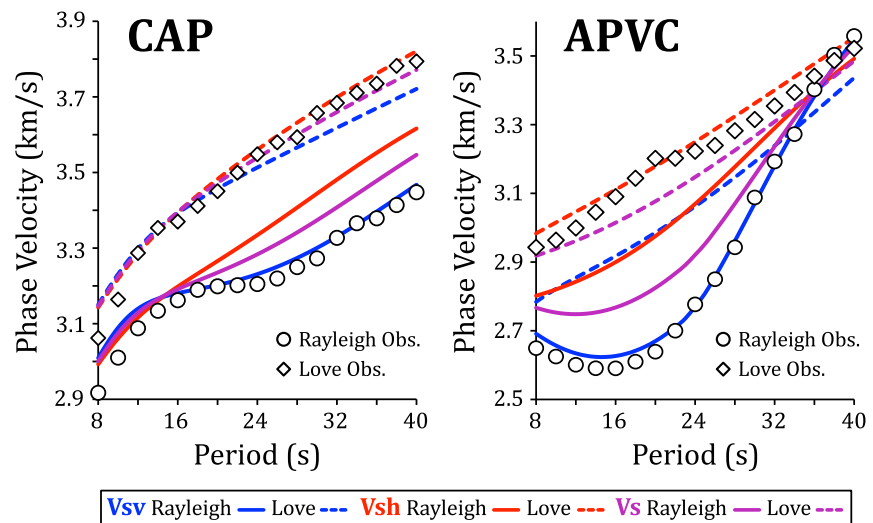


**Figure 9.** Forward modeled dispersion for Rayleigh (solid lines) and Love (dashed lines) waves for  $V_{sh}$  (red),  $V_{sv}$  (blue), and average  $V_s$  ( $V_{sh} + V_{sv}/2$ ; purple) models for characteristic locations in the CAP and APVC. Observed phase velocity measurements are shown as circles for Rayleigh waves and diamonds for Love waves.

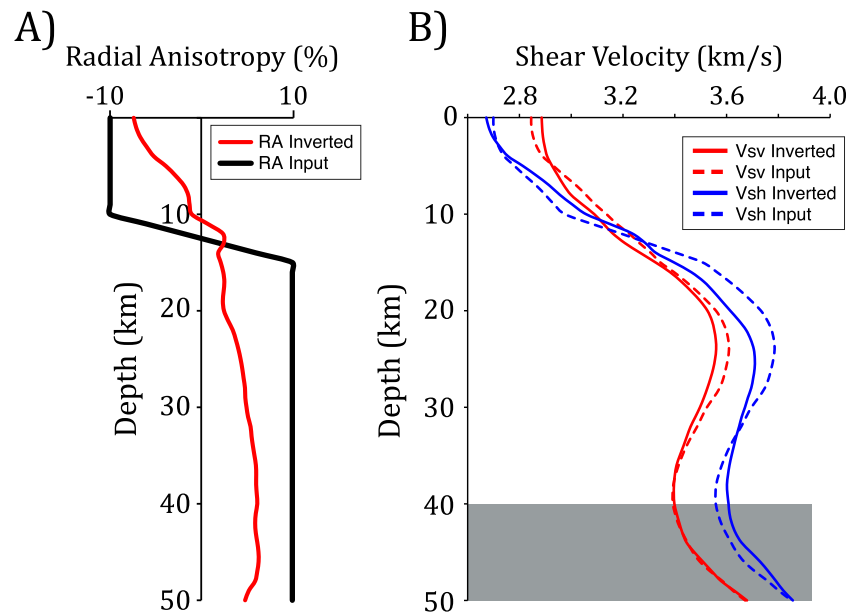


**Figure 10.** (a) Input radial anisotropy model with a  $-10\%$  layer in the upper 10 km transitioning to  $+10\%$  at depths below 15 km (black), and our inverted (red) radial anisotropy results. (b) Input (dashed) and inverted (solid)  $V_{sv}$  (red) and  $V_{sh}$  (blue) models (based on average CAP velocities in the upper 50 km and PREM, Dziewonski & Anderson, 1981, at deeper depths) with the depths outside of which we have sensitivity obscured.

$V_{sv}$  and  $V_{sh}$  models show good agreement, exhibiting similar spatial patterns in shear velocity throughout the Andean crust (Figures 6, 7, and 8). This is unsurprising given that, with the exception of radial anisotropy, they reflect the same velocity structures. The  $V_{sv}$  and  $V_{sh}$  models begin to deviate at deeper depths due to the different sensitivity kernels of Love and Rayleigh waves. At the periods used in this study, resolution of Love waves (and therefore the  $V_{sh}$  and radial anisotropy models) is restricted to the upper  $\sim 40$  km, while Rayleigh (and therefore the  $V_{sv}$  model) sensitivity extends to  $\sim 50$  km (Figures S1, S6, and S7). The  $V_{sh}$  and  $V_{sv}$  models also have different ray path densities (Figure 3) owing to the quality control steps described above. Horizontal component-derived cross correlations (such as TT) are generally noisier (sporadic noise not ambient noise) than those derived from the vertical components (ZZ). This leads to fewer TT cross correlations passing the  $>10$  SNR quality control filter.

We performed jackknife tests of our  $V_{sv}$  and  $V_{sh}$  models, throwing out 10% of interstation paths for each period for each iteration. Examples of jackknifed phase velocity maps along with maps of standard deviations of phase velocities can be seen in Figures S8–S15. In general, phase velocity standard deviations are less than 0.05 km/s for ZZ components and 0.07 km/s for TT components, with the highest standard deviations occurring at the shortest periods (Figures S8–S15). We then inverted the jackknifed phase velocities for  $V_{sh}$  and  $V_{sv}$  following the steps described above. Below  $\sim 10$  km depth our results are very robust (Figures 6 and 8). In the upper  $\sim 10$  km there is more variance in the  $V_{sh}$  and  $V_{sv}$  models, making inferences of radial anisotropy a bit more speculative. We also performed a synthetic test of our radial anisotropy results (Figure 10) using the Mineos software package (Masters et al., 2011). We calculated Rayleigh and Love dispersion curves for a model similar to that observed beneath the CAP. We then inverted for  $V_{sh}$ ,  $V_{sv}$ , and RA following our inversion scheme, which initially assumes an isotropic starting model. We find that inverting for  $V_{sh}$  and  $V_{sv}$  separately produces shear velocity and radial anisotropy results that match our input model reasonably well, even underestimating radial anisotropy at midcrustal depths (Figure 10). The synthetic  $V_{sh}$  model exhibits larger deviations from the input model than the  $V_{sv}$  model. At depths below  $\sim 30$  km, the inverted  $V_{sh}$  model begins to overestimate the input shear velocity, while at depth shallower than  $\sim 30$  km,  $V_{sh}$  is underestimated. The differences we observe between the input and inverted  $V_{sh}$  models make interpreting absolute radial anisotropy percentages a challenge, so we therefore only interpret patterns of radial anisotropy moving forward.

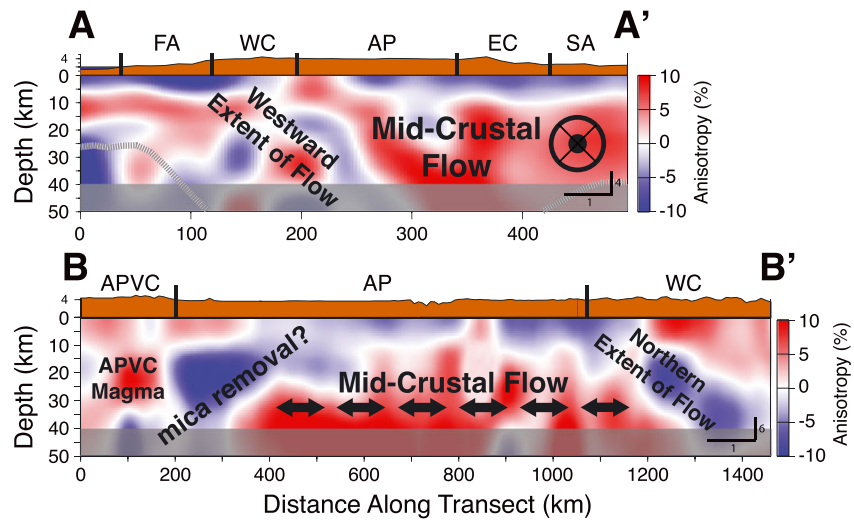


**Figure 11.** Schematic of our preferred interpretation of the radial anisotropy beneath the Altiplano.

## 5. Discussion

Beneath the Altiplano, we see positive radial anisotropy at midcrustal depths (Figures 6 and 7). In cross section A to A', which runs orthogonally to the trench through the CAP (Figure 6), we observe positive radial anisotropy eastward of the subducting slab. While we do not have resolution eastward of the Eastern Cordillera, beneath the Altiplano and the majority of the Eastern Cordillera positive radial anisotropy dominates at midcrustal depths. When looking along the length of the CAP (cross section B to B'; Figure 7), midcrustal positive radial anisotropy is observed beneath the entire physiographic Altiplano province. Taking cross sections A-A' and B-B' in concert, it is clear that the vast majority of midcrust beneath the Altiplano is characterized by positive radial anisotropy. The extent and consistency of the anisotropic region suggests that we are observing a consistent widespread crustal feature.

We interpret the positive radial anisotropy beneath the Altiplano as the result of deformation-induced alignment of micas due to lateral ductile crustal flow (Figure 11). This region of positive anisotropy is not strongly associated with a major low-velocity anomaly in either the  $V_{sh}$  or  $V_{sv}$  models making a magmatic source unlikely. There is, however, an active arc on the western edge of the CAP, and we can therefore not completely rule out magmatism as a source of positive radial anisotropy.

The depth to the top of the positive radial anisotropy varies, but it generally lies between ~10- and 20-km depth. This corresponds to the top of the Andean low-velocity zone identified in receiver function studies across much of the Altiplano (Beck & Zandt, 2002; Ryan et al., 2016; Yuan et al., 2000). This may correspond to the brittle-ductile transition in the CAP crust. Unfortunately, there is a lack of well-located crustal earthquakes in the area surrounding our observed positive radial anisotropy. If the top of the anisotropic feature truly represents ductile crustal behavior, we would expect to see a dramatic decrease in crustal earthquakes with the emergence of positive anisotropy. This remains an area of future research. Due to the depth limitations of the  $V_{sh}$  shear velocity model, we do not have resolution of the lower boundary of the radial anisotropy. Ductile crustal flow may extend to the Moho or merely to lower-crustal depths below the resolution of our models.

Since observations of radial anisotropy do not carry directional information, we cannot make definitive assertions about the direction of crustal flow from our models. Taking insights from the local geologic setting, however, we propose that crustal material is likely being evacuated in a north-south orientation, which is consistent with previous studies (Eichelberger et al., 2015; Kley & Monaldi, 1998; McQuarrie et al., 2005; Oncken et al., 2006; Schepers et al., 2017). Although we do not have resolution east of the Eastern Cordillera, it is unlikely that crustal material is escaping eastward toward the South American interior. If crustal material were escaping eastward, we would expect gentler topographic gradients in the Eastern Cordillera similar to those seen surrounding the Tibetan plateau (e.g., Clark & Royden, 2000; Royden et al., 1997). If

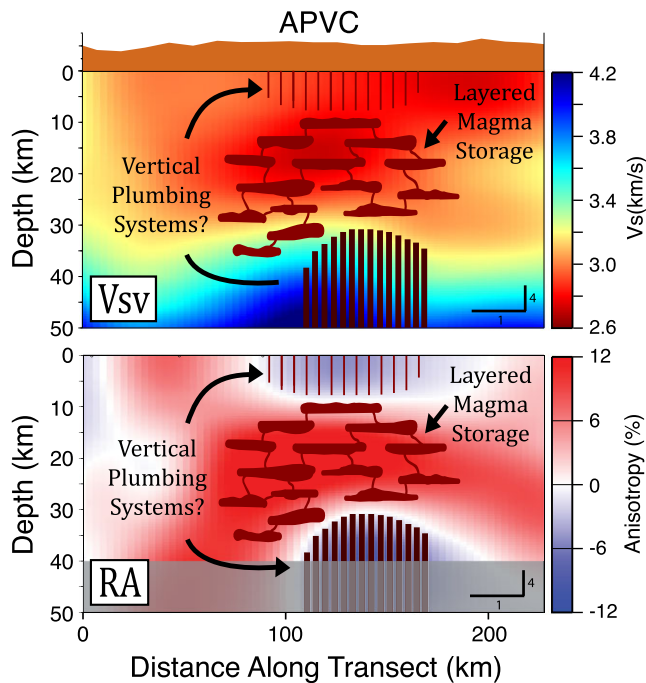


**Figure 12.** Schematic of our preferred interpretation of the radial anisotropy beneath the APVC. The region of extremely strong positive radial anisotropy coincides closely with the low-velocity anomaly beneath the APVC. We suggest this is due to a horizontally aligned magma storage system in the crust.

the crust associated with the South American cratonic interior is stronger than that in the Altiplano (e.g., Beck & Zandt, 2002), it may act as an eastern barrier to flow. Crustal flow does not seem to extend west of the CAP into the Western Cordillera or the fore-arc regions based on the lack of coherent radial anisotropy. The presence of the subducting Nazca slab represents a barrier to westward crustal flow.

With potential barriers to the east and west, we suggest that crustal material is being forced along the north–south axis of the CAP. To the north of the Altiplano, flat slab subduction beneath Peru may inhibit significant northward extrusion of crustal material. With the subducting slab impinging upon the bottom of overriding plate, it may be difficult to create space to accommodate large amounts of intruded material. Changes in basement composition, thermal structure, and/or the Abancay deflection (e.g., Roperch et al., 2011) may also act as potential barriers to northward flow. We have no constraints on radial anisotropy from our models south of the APVC. Throughout the Central Andes, there are no obvious surface indications of ductile crustal flow escaping from the region like those exhibited in Tibet by the varying topographic gradients (e.g., Clark & Royden, 2000; Royden et al., 1997). It may be that crustal flow escaping from the CAP has yet to manifest topographic observables beyond a relatively flat CAP. The lack of topographic evidence of crustal flow may arise for a variety of reasons that require further study, such as variations in crustal composition, thermal structure, amounts of shortening, and/or tectonic history. Our suggested north–south crustal flow is highly speculative and requires expanded studies both to the north and south of the CAP.

Two regions of negative radial anisotropy bound the Altiplano-related region of positive radial anisotropy. The emergence of the northern negative anisotropic anomaly coincides closely with northernmost expression of the Altiplano (Figure 7). North of the Altiplano, the Andes become far narrower (with the Eastern and Western Cordillera no longer separated) and crustal thicknesses are slightly reduced (to ~60 km). Due to the relatively narrow extent of the Andes, there may be insufficiently thick crustal material to facilitate extensive lateral crustal flow. This would allow structural signals, such as those from faults and/or cracks, or the vertical alignment of anisotropic minerals to emerge.

The second region of negative radial anisotropy lies to the south of the Altiplano. This anisotropic structure roughly corresponds to the boundary between the Altiplano and Puna plateaus and separates regions of positive radial anisotropy associated with the Altiplano and the APVC. Thick crust is present beneath the entirety of this region, so it is unlikely that faulting and folding be solely responsible for the negative anisotropy if ductile flow dominates to the north. Unlike the majority of the Altiplano, the southernmost Altiplano and northernmost Puna is characterized by extensive volcanism, exemplified by the APVC (e.g., Kay et al., 2010; Salisbury et al., 2010). Significant amounts of melt can drastically alter patterns of radial anisotropy in the crust through the alteration and/or removal of micas (e.g., Almqvist et al., 2015; Schmidt et al., 2004). The removal of mica-related anisotropy allows the emergence of anisotropy due to other mineral phases or preexisting fabrics and structures. We interpret the southern negative anisotropic feature as a region where micas have been removed. We are likely observing either a structural signal or anisotropy due to amphiboles or other anisotropic mineral phases.

Beneath the APVC lies a region of very slow shear velocities and very strong positive radial anisotropy (Figure 8). The APVC is home to vast amounts of volcanism and an extensive magmatic storage system (e.g., Ward et al., 2014). Positive radial anisotropy beneath the APVC is therefore most likely due to a horizontally aligned magma storage system in the crust. Horizontally aligned melt lenses (through a network of connected sills) can create a layered system with contrasting elastic properties that would result in the observed positive anisotropy. Velocity profiles with depth through the APVC further support a melt-generated source of anisotropy (Figure 8b). Beneath the APVC,  $V_{sv}$  shows a much larger velocity reduction than  $V_{sh}$ . This is

typical of melt-induced radial anisotropy (e.g., Kawakatsu et al., 2009; Takeuchi et al., 1968). We suggest that the positive anisotropy associated with the slow velocity anomaly beneath the APVC comes from the horizontal alignment of melt pockets in the crust, while the regions of negative radial anisotropy above and below may be indicative of the plumbing structures that feed the magma body from below and export magmatic material to the surface (Figure 12).

An important limitation of our  $V_{sh}$  and radial anisotropy models is that they are only sensitive between depths of ~4 km to ~40 km. This prevents us from imaging patterns of radial anisotropy in the lower crust beneath the majority of the CAP. We are unable to assess whether ductile crustal deformation beneath the Altiplano extends to the Moho or merely to the bottom of our model. This shortcoming is particularly acute when trying to determine the direction of crustal flow beneath the Altiplano. Since we cannot observe shear wave velocities down to the Moho, it is possible that the behavior of the lower crust is different than that of the midcrust.

## 6. Summary

We invert both Love and Rayleigh wave EGFs from ambient noise data for  $V_{shr}$ ,  $V_{svr}$ , and radial anisotropy throughout the Central Andes. Beneath the Altiplano, we observe widespread positive radial anisotropy throughout the midcrust likely indicative of ductile crustal deformation. Our results suggest that beneath the Altiplano, ductile crustal flow in the midcrust is widespread and begins at depths of ~10–20 km. To the south of the Altiplano beneath the APVC, we see a region characterized by very slow shear velocities and very strong positive radial anisotropy. This likely reflects horizontally aligned melt structures that comprise the magma storage system beneath the APVC.

### Acknowledgments

Data were obtained via the Data Management Center of the Incorporated Research Institutions for Seismology and the European Integrated Data Archive for seismic networks: C (Lange et al., 2016), C1 (Universidad de Chile, 2013), CX (GFZ and CNRS-INSU, 2006), GE (GEOFON Data Centre, 1993), GT (ASL and USGS, 1993), II (Scripps Institution of Oceanography, 1986), TO (PeruSE, 2013), XE (Silver et al., 1994), XP (West & Christensen, 2010), Y9 (Peyrat et al., 2010), ZA (Asch et al., 2002), ZD (Wagner et al., 2010), ZE (Haberland et al., 1996), and ZG (Beck et al., 2010). This work was funded by NSF EAR-1415914. Several figures were made using Generic Mapping Tools (Wessel & Smith, 1991). We thank two anonymous reviewers for their comments.

### References

- Allmendinger, R. W., Jordan, T. E., Kay, S. M., & Isacks, B. L. (1997). The evolution of the Altiplano-Puna plateau of the Central Andes. *Annual Review of Earth and Planetary Sciences*, 25(1), 139–174. <https://doi.org/10.1146/annurev.earth.25.1.139>
- Almqvist, B. S., Misra, S., Klonowska, I., Mainprice, D., & Majka, J. (2015). Ultrasonic velocity drops and anisotropy reduction in mica-schist analogues due to melting with implications for seismic imaging of continental crust. *Earth and Planetary Science Letters*, 425, 24–33. <https://doi.org/10.1016/j.epsl.2015.05.039>
- Amante, C., & Eakins, B. W. (2009). ETOPO1 1 arc-minute global relief model: Procedures, data sources and analysis. NOAA Technical Memorandum NESDIS NGDC-24. National Geophysical Data Center, NOAA. <https://doi.org/10.7289/V5C8276M>
- Asch, G., Heit, B., & Yuan, X. (2002). The ReFuCA project: Receiver functions Central Andes. Deutsches GeoForschungsZentrum GFZ. Other/Seismic Network. <https://doi.org/10.14470/MN7557778612>
- ASL and USGS (1993). Global telemetered seismograph network (USAF/USGS). International Federation of Digital Seismograph Networks. Other/Seismic Network. <https://doi.org/10.7914/SN/GT>
- Assumpção, M., Feng, M., Tassara, A., & Julià, J. (2013). Models of crustal thickness for South America from seismic refraction, receiver functions and surface wave tomography. *Tectonophysics*, 609, 82–96. <https://doi.org/10.1016/j.tecto.2012.11.014>
- Barmin, M. P., Ritzwoller, M. H., & Levshin, A. L. (2001). A fast and reliable method for surface wave tomography. In *Monitoring the Comprehensive Nuclear-Test-Ban Treaty: Surface Waves* (pp. 1351–1375). Basel: Birkhäuser. [https://doi.org/10.1007/978-3-0348-8264-4\\_3](https://doi.org/10.1007/978-3-0348-8264-4_3)
- Beaumont, C., Jamieson, R. A., Nguyen, M. H., & Lee, B. (2001). Himalayan tectonics explained by extrusion of a low-viscosity crustal channel coupled to focused surface denudation. *Nature*, 414(6865), 738–742. <https://doi.org/10.1038/414738a>
- Beaumont, C., Nguyen, M. H., Jamieson, R. A., & Ellis, S. (2006). Crustal flow modes in large hot orogens. *Geological Society of London, Special Publications*, 268(1), 91–145. <https://doi.org/10.1144/GSL.SP.2006.268.01.05>
- Beck, S. L., & Zandt, G. (2002). The nature of orogenic crust in the Central Andes. *Journal of Geophysical Research*, 107(B10), 2230. <https://doi.org/10.1029/2000JB000124>
- Beck, S. L., Zandt, G., Myers, S. C., Wallace, T. C., Silver, P. G., & Drake, L. (1996). Crustal-thickness variations in the Central Andes. *Geology*, 24(5), 407–410. [https://doi.org/10.1130/0091-7613\(1996\)E2%80%8B024%3C0407:CTVITC%3E%2%80%8B2.3.CO;2](https://doi.org/10.1130/0091-7613(1996)E2%80%8B024%3C0407:CTVITC%3E%2%80%8B2.3.CO;2)
- Beck, S. L., Zandt, G., & Wagner, L. (2010). Central Andean uplift and the geodynamics of the high topography. International Federation of Digital Seismograph Networks. Other/Seismic Network. [https://doi.org/10.7914/SN/ZG\\_2010](https://doi.org/10.7914/SN/ZG_2010)
- Bensen, G. D., Ritzwoller, M. H., & Shapiro, N. M. (2008). Broadband ambient noise surface wave tomography across the United States. *Journal of Geophysical Research*, 113, B05306. <https://doi.org/10.1029/2007JB005248>
- Bensen, G. D., Ritzwoller, M. H., & Yang, Y. (2009). A 3-D shear velocity model of the crust and uppermost mantle beneath the United States from ambient seismic noise. *Geophysical Journal International*, 177(3), 1177–1196. <https://doi.org/10.1111/j.1365-246X.2009.04125.x>
- Cahill, T., & Isacks, B. L. (1992). Seismicity and shape of the subducted Nazca plate. *Journal of Geophysical Research*, 97(B12), 17,503–17,529. <https://doi.org/10.1029/92JB00493>
- Chen, H., Zhu, L., & Su, Y. (2016). Low velocity crustal flow and crust–mantle coupling mechanism in Yunnan, SE Tibet, revealed by 3D S-wave velocity and azimuthal anisotropy. *Tectonophysics*, 685, 8–20. <https://doi.org/10.1016/j.tecto.2016.07.007>
- Cheng, C., Chen, L., Yao, H. J., Jiang, M. M., & Wang, B. Y. (2013). Distinct variations of crustal shear wave velocity structure and radial anisotropy beneath the North China craton and tectonic implications. *Gondwana Research*, 23(1), 25–38. <https://doi.org/10.1016/j.gr.2012.02.014>
- Chmielowski, J., Zandt, G., & Haberland, C. (1999). The central Andean Altiplano-Puna magma body. *Geophysical Research Letters*, 26(6), 783–786. <https://doi.org/10.1029/1999GL900078>

- Clark, M. K., & Royden, L. H. (2000). Topographic ooze: Building the eastern margin of Tibet by lower crustal flow. *Geology*, 28(8), 703–706. [https://doi.org/10.1130/0091-7613\(2000\)E2%80%8B28%3C703:TOBTEM%3E%2%80%8B2.0.CO;2](https://doi.org/10.1130/0091-7613(2000)E2%80%8B28%3C703:TOBTEM%3E%2%80%8B2.0.CO;2)
- Crampin, S. (1981). A review of wave motion in anisotropic and cracked elastic-media. *Wave Motion*, 3(4), 343–391. [https://doi.org/10.1016/0165-2125\(81\)90026-3](https://doi.org/10.1016/0165-2125(81)90026-3)
- Crampin, S. (1984). Effective anisotropic elastic constants for wave propagation through cracked solids. *Geophysical Journal of the Royal Astronomical Society*, 76(1), 135–145. <https://doi.org/10.1111/j.1365-246X.1984.tb05029.x>
- Crampin, S. (1987). The geological and industrial implication of extensive dilatancy anisotropy. *Nature*, 328(6130), 491–496. <https://doi.org/10.1038/328491a0>
- Crampin, S., & Lovell, J. H. (1991). A decade of shear-wave splitting in the earth's crust: What does it mean? What use can we make of it? And what should we do next? *Geophysical Journal International*, 107(3), 387–407. <https://doi.org/10.1111/j.1365-246X.1991.tb01401.x>
- De Silva, S., Zandt, G., Trumbull, R., Viramonte, J. G., Salas, G., & Jiménez, N. (2006). Large ignimbrite eruptions and volcano-tectonic depressions in the Central Andes: A thermomechanical perspective. *Geological Society of London, Special Publications*, 269(1), 47–63. <https://doi.org/10.1144/GSL.SP.2006.269.01.04>
- De Silva, S. L. (1989). Altiplano-Puna volcanic complex of the Central Andes. *Geology*, 17(12), 1102–1106. [https://doi.org/10.1130/0091-7613\(1989\)E2%80%8B017%3C1102:APVOT%3E%2%80%8B2.3.CO;2](https://doi.org/10.1130/0091-7613(1989)E2%80%8B017%3C1102:APVOT%3E%2%80%8B2.3.CO;2)
- DeMets, C., Gordon, R. G., & Argus, D. F. (2010). Geologically current plate motions. *Geophysical Journal International*, 181(1), 1–80. <https://doi.org/10.1111/j.1365-246X.2009.04491.x>
- Dziewonski, A. M., & Anderson, D. L. (1981). Preliminary reference Earth model. *Physics of the Earth and Planetary Interiors*, 25(4), 297–356. [https://doi.org/10.1016/0031-9201\(81\)90046-7](https://doi.org/10.1016/0031-9201(81)90046-7)
- Echavarría, L., Hernández, R., Allmendinger, R., & Reynolds, J. (2003). Subandean thrust and fold belt of northwestern Argentina: Geometry and timing of the Andean evolution. *AAPG Bulletin*, 87(6), 965–985. <https://doi.org/10.1306/01200300196>
- Eichelberger, N., McQuarrie, N., Ryan, J., Karimi, B., Beck, S. L., & Zandt, G. (2015). Evolution of crustal thickening in the Central Andes, Bolivia. *Earth and Planetary Science Letters*, 426, 191–203. <https://doi.org/10.1016/j.epsl.2015.06.035>
- Fichtner, A. (2014). Source and processing effects on noise correlations. *Geophysical Journal International*, 197(3), 1527–1531. <https://doi.org/10.1093/gji/ggu093>
- Fichtner, A. (2015). Source-structure trade-offs in ambient noise correlations. *Geophysical Journal International*, 202(1), 678–694. <https://doi.org/10.1093/gji/ggv182>
- Fielding, E., Isacks, B., Barazangi, M., & Duncan, C. (1994). How flat is Tibet? *Geology*, 22(2), 163–167. [https://doi.org/10.1130/0091-7613\(1994\)E2%80%8B022%3C0163:HFIT%3E%2%80%8B2.3.CO;2](https://doi.org/10.1130/0091-7613(1994)E2%80%8B022%3C0163:HFIT%3E%2%80%8B2.3.CO;2)
- Garzone, C. N., McQuarrie, N., Perez, N. D., Ehlers, T. A., Beck, S. L., Kar, N., et al. (2017). Tectonic evolution of the Central Andean plateau and implications for the growth of plateaus. *Annual Review of Earth and Planetary Sciences*, 45(1), 529–559. <https://doi.org/10.1146/annurev-earth-063016-020612>
- GEOFON Data Centre (1993). GEOFON seismic network. Deutsches GeoForschungsZentrum GFZ. Other/Seismic Network. <https://doi.org/10.14470/TR560404>
- Gerbault, M., Martinod, J., & Héral, G. (2005). Possible orogeny-parallel lower crustal flow and thickening in the Central Andes. *Tectonophysics*, 399(1–4), 59–72. <https://doi.org/10.1016/j.tecto.2004.12.015>
- GFZ and CNRS-INSU (2006). Integrated Plate boundary Observatory Chile - IPOC. International Federation of Digital Seismograph Networks Other/Seismic Network. <https://doi.org/10.14470/PK615318>
- Gotberg, N., McQuarrie, N., & Caillaux, V. C. (2010). Comparison of crustal thickening budget and shortening estimates in southern Peru (12–14°S): Implications for mass balance and rotations in the “Bolivian orocline”. *Geological Society of America Bulletin*, 122(5–6), 727–742. <https://doi.org/10.1130/B26477.1>
- Gripp, A. E., & Gordon, R. G. (2002). Young tracks of hotspots and current plate velocities. *Geophysical Journal International*, 150(2), 321–361. <https://doi.org/10.1046/j.1365-246X.2002.01627.x>
- Gubbels, T. L., Isacks, B. L., & Farrar, E. (1993). High-level surfaces, plateau uplift, and foreland development, Bolivian Central Andes. *Geology*, 21(8), 695–698. [https://doi.org/10.1130/0091-7613\(1993\)E2%80%8B021%3C0695:HLSPUA%3E%2%80%8B2.3.CO;2](https://doi.org/10.1130/0091-7613(1993)E2%80%8B021%3C0695:HLSPUA%3E%2%80%8B2.3.CO;2)
- Guo, Z., Gao, X., Wang, W., & Yao, Z. (2012). Upper-and mid-crustal radial anisotropy beneath the central Himalaya and southern Tibet from seismic ambient noise tomography. *Geophysical Journal International*, 189(2), 1169–1182. <https://doi.org/10.1111/j.1365-246X.2012.05425.x>
- Guo, Z., Yang, Y., & Chen, Y. (2016). Crustal radial anisotropy in Northeast China and its implications for the regional tectonic extension. *Geophysical Journal International*, 207(1), 197–208. <https://doi.org/10.1093/gji/ggv261>
- Haberland, C., Rietbrock, A., Asch, G., & Chong, C. (1996). The ANCORP Seismic Network. Deutsches GeoForschungsZentrum GFZ. Other/Seismic Network. <https://doi.org/10.14470/mr6441682066>
- Hayes, G. P., Wald, D. J., & Johnson, R. L. (2012). Slab1. 0: A three-dimensional model of global subduction zone geometries. *Journal of Geophysical Research*, 117, B01302. <https://doi.org/10.1029/2011JB008524>
- Heit, B., Bianchi, M., Yuan, X., Kay, S. M., Sandvol, E., Kumar, P., et al. (2014). Structure of the crust and the lithosphere beneath the southern Puna plateau from teleseismic receiver functions. *Earth and Planetary Science Letters*, 385, 1–11. <https://doi.org/10.1016/j.epsl.2013.10.017>
- Herrmann, R. B. (2013). Computer programs in seismology: An evolving tool for instruction and research. *Seismological Research Letters*, 84(6), 1081–1088. <https://doi.org/10.1785/0220110096>
- Hindle, D., Kley, J., Oncken, O., & Sobolev, S. (2005). Crustal balance and crustal flux from shortening estimates in the Central Andes. *Earth and Planetary Science Letters*, 230(1–2), 113–124. <https://doi.org/10.1016/j.epsl.2004.11.004>
- Holtzman, B. K., Kohlstedt, D. L., Zimmerman, M. E., Heidelbach, F., Hiraga, T., & Hufstodt, J. (2003). Melt segregation and strain partitioning: Implications for seismic anisotropy and mantle flow. *Science*, 301(5637), 1227–1230. <https://doi.org/10.1126/science.1087132>
- Horton, B. K., & DeCelles, P. G. (1997). The modern foreland basin system adjacent to the Central Andes. *Geology*, 25(10), 895–898. [https://doi.org/10.1130/0091-7613\(1997\)E2%80%8B025%3C0895:TMFBASA%3E%2%80%8B2.3.CO;2](https://doi.org/10.1130/0091-7613(1997)E2%80%8B025%3C0895:TMFBASA%3E%2%80%8B2.3.CO;2)
- Huang, H., Yao, H., & van der Hilst, R. D. (2010). Radial anisotropy in the crust of SE Tibet and SW China from ambient noise interferometry. *Geophysical Research Letters*, 37, L21310. <https://doi.org/10.1029/2010GL044981>
- Husson, L., & Sempere, T. (2003). Thickening the Altiplano crust by gravity-driven crustal channel flow. *Geophysical Research Letters*, 30(5), 1243. <https://doi.org/10.1029/2002GL016877>
- Isacks, B. L. (1988). Uplift of the central Andean plateau and bending of the Bolivian orocline. *Journal of Geophysical Research*, 93(B4), 3211–3231. <https://doi.org/10.1029/JB093iB04p03211>
- Jiang, C., Yang, Y., Rawlinson, N., & Griffin, W. L. (2016). Crustal structure of the Newer Volcanics Province, SE Australia, from ambient noise tomography. *Tectonophysics*, 687, 257–267. <https://doi.org/10.1016/j.tecto.2016.06.003>

- Karato, S. I. (2012). *Deformation of Earth materials: An introduction to the rheology of solid earth*. Cambridge, UK: Cambridge University Press.
- Kawakatsu, H., Kumar, P., Takei, Y., Shinohara, M., Kanazawa, T., Araki, E., & Suyehiro, K. (2009). Seismic evidence for sharp lithosphere-asthenosphere boundaries of oceanic plates. *Science*, *324*(5926), 499–502. <https://doi.org/10.1126/science.1169499>
- Kay, S. M., Coira, B. L., Caffè, P. J., & Chen, C. H. (2010). Regional chemical diversity, crustal and mantle sources and evolution of central Andean Puna plateau ignimbrites. *Journal of Volcanology and Geothermal Research*, *198*(1–2), 81–111. <https://doi.org/10.1016/j.jvolgeores.2010.08.013>
- Kendrick, E., Bevis, M., Smalley, R., & Brooks, B. (2001). An integrated crustal velocity field for the central Andes. *Geochemistry, Geophysics, Geosystems*, *2*(11), 1066. <https://doi.org/10.1029/2001GC000191>
- Kennett, B. L. N., Engdahl, E. R., & Buland, R. (1995). Constraints on seismic velocities in the Earth from travel times. *Geophysical Journal International*, *122*(1), 108–124. <https://doi.org/10.1111/j.1365-246X.1995.tb03540.x>
- Kley, J., & Monaldi, C. R. (1998). Tectonic shortening and crustal thickness in the Central Andes: How good is the correlation? *Geology*, *26*(8), 723–726. [https://doi.org/10.1130/0091-7613\(1998\)026%3C0723:TSACTI%3E2.3.CO;2](https://doi.org/10.1130/0091-7613(1998)026%3C0723:TSACTI%3E2.3.CO;2)
- Kley, J., Monaldi, C. R., & Salfity, J. A. (1999). Along-strike segmentation of the Andean foreland: Causes and consequences. *Tectonophysics*, *301*(1–2), 75–94. [https://doi.org/10.1016/S0040-1951\(98\)90223-2](https://doi.org/10.1016/S0040-1951(98)90223-2)
- Lamb, S., & Hoke, L. (1997). Origin of the high plateau in the Central Andes, Bolivia, South America. *Tectonics*, *16*(4), 623–649. <https://doi.org/10.1029/97TC00495>
- Lange, D., Geersen, J., Barrientos, S., Moreno, M., Grevemeyer, I., Contreras-Reyes, E., & Kopp, H. (2016). Aftershock seismicity and tectonic setting of the 2015 September 16 *M*<sub>w</sub> 8.3 Illapel earthquake, Central Chile. *Geophysical Journal International*, *206*(2), 1424–1430. <https://doi.org/10.1093/gji/ggw218>
- Leary, P. C., Crampin, S., & McEvilly, T. V. (1990). Seismic fracture anisotropy in the Earth's crust: an overview. *Journal of Geophysical Research*, *95*, 11,105–11,114. <https://doi.org/10.1029/JB095iB07p11105>
- Levshin, A., Ratnikova, L., & Berger, J. (1992). Peculiarities of surface-wave propagation across central Eurasia. *Bulletin of the Seismological Society of America*, *82*(6), 2464–2493.
- Lin, F. C., Moschetti, M. P., & Ritzwoller, M. H. (2008). Surface wave tomography of the western United States from ambient seismic noise: Rayleigh and love wave phase velocity maps. *Geophysical Journal International*, *173*(1), 281–298. <https://doi.org/10.1111/j.1365-246X.2008.03720.x>
- Ling, Y., Chen, L., Wei, Z., Jiang, M., & Wang, X. (2017). Crustal S-velocity structure and radial anisotropy beneath the southern part of central and western North China craton and the adjacent Qilian Orogenic Belt from ambient noise tomography. *Science China Earth Sciences*, *60*(10), 1752–1768. <https://doi.org/10.1007/s11430-017-9092-8>
- Lloyd, G. E., Butler, R. W. H., Casey, M., & Mainprice, D. (2009). Mica, deformation fabrics and the seismic properties of the continental crust. *Earth and Planetary Science Letters*, *288*(1–2), 320–328. <https://doi.org/10.1016/j.epsl.2009.09.035>
- Luo, Y., Xu, Y., & Yang, Y. (2013). Crustal radial anisotropy beneath the Dabie orogenic belt from ambient noise tomography. *Geophysical Journal International*, *195*(2), 1149–1164. <https://doi.org/10.1093/gji/ggt281>
- Luo, Y., Yang, Y., Xu, Y., Xu, H., Zhao, K., & Wang, K. (2015). On the limitations of interstation distances in ambient noise tomography. *Geophysical Journal International*, *201*(2), 652–661. <https://doi.org/10.1093/gji/ggv043>
- Lynner, C., Anderson, M. L., Portner, D. E., Beck, S. L., & Gilbert, H. (2017). Mantle flow through a tear in the Nazca slab inferred from shear wave splitting. *Geophysical Research Letters*, *44*, 6735–6742. <https://doi.org/10.1002/2017GL074312>
- Lynner, C., & Porritt, R. W. (2017). Crustal structure across the eastern north American margin from ambient noise tomography. *Geophysical Research Letters*, *44*, 6651–6657. <https://doi.org/10.1002/2017GL073500>
- Mahan, K. (2006). Retrograde mica in deep crustal granulites: Implications for crustal seismic anisotropy. *Geophysical Research Letters*, *33*, L24301. <https://doi.org/10.1029/2006GL028130>
- Mainprice, D., & Nicolas, A. (1989). Development of shape and lattice preferred orientations: Application to the seismic anisotropy of the lower crust. *Journal of Structural Geology*, *11*(1–2), 175–189. [https://doi.org/10.1016/0191-8141\(89\)90042-4](https://doi.org/10.1016/0191-8141(89)90042-4)
- Mamani, M., Wörner, G., & Sempere, T. (2010). Geochemical variations in igneous rocks of the Central Andean orocline (13°S to 18°S): Tracing crustal thickening and magma generation through time and space. *Geological Society of America Bulletin*, *122*(1–2), 162–182. <https://doi.org/10.1130/B26538.1>
- Masters, G., Woodhouse, J. H., & Freeman, G. (2011). Mineos v1.0.2 [software], Computational Infrastructure for Geodynamics. Retrieved from <https://geodynamics.org/cig/software/mineos/>
- McQuarrie, N., Horton, B. K., Zandt, G., Beck, S. L., & DeCelles, P. G. (2005). Lithospheric evolution of the Andean fold-thrust belt, Bolivia, and the origin of the central Andean plateau. *Tectonophysics*, *399*(1–4), 15–37. <https://doi.org/10.1016/j.tecto.2004.12.013>
- Meissner, R., Rabbal, W., & Kern, H. (2006). Seismic lamination and anisotropy of the lower continental crust. *Tectonophysics*, *416*(1–4), 81–99. <https://doi.org/10.1016/j.tecto.2005.11.013>
- Moschetti, M. P., Ritzwoller, M. H., Lin, F. C., & Yang, Y. (2010). Seismic evidence for widespread western-US deep-crustal deformation caused by extension. *Nature*, *464*(7290), 885–889. <https://doi.org/10.1038/nature08951>
- Nishizawa, O., & Yoshino, T. (2001). Seismic velocity anisotropy in mica-rich rocks: An inclusion model. *Geophysical Journal International*, *145*(1), 19–32. <https://doi.org/10.1111/j.1365-246X.2001.00331.x>
- Norabuena, E., Leffler-Griffin, L., Mao, A., Dixon, T., Stein, S., Sacks, I. S., et al. (1998). Space geodetic observations of Nazca-South America convergence across the Central Andes. *Science*, *279*(5349), 358–362. <https://doi.org/10.1126/science.279.5349.358>
- Ojo, A. O., Ni, S., & Li, Z. (2017). Crustal radial anisotropy beneath Cameroon from ambient noise tomography. *Tectonophysics*, *696*–697, 37–51. <https://doi.org/10.1016/j.tecto.2016.12.018>
- Oncken, O., Hindle, D., Kley, J., Elger, K., Victor, P., & Schemmann, K. (2006). Deformation of the central Andean upper plate system—Facts, fiction, and constraints for plateau models. In *The Andes* (pp. 3–27). Berlin: Springer. [https://doi.org/10.1007/978-3-540-48684-8\\_1](https://doi.org/10.1007/978-3-540-48684-8_1)
- Quimet, W. B., & Cook, K. L. (2010). Building the Central Andes through axial lower crustal flow. *Tectonics*, *29*, TC3010. <https://doi.org/10.1029/2009TC002460>
- Pawlak, A., Eaton, D. W., Darbyshire, F., Lebedev, S., & Bastow, J. D. (2012). Crustal anisotropy beneath Hudson Bay from ambient noise tomography: Evidence for post-orogenic lower-crustal flow? *Journal of Geophysical Research*, *117*, B08301. <https://doi.org/10.1029/2011JB009066>
- PeruSE (2013). Peru subduction experiment. Caltech. Other/Seismic Network. <https://doi.org/10.7909/C3H41PBZ>
- Peyrat, S., Madariaga, R., Buforn, E., Campos, J., Asch, G., & Vilotte, J. P. (2010). Kinematic rupture process of the 2007 Tocopilla earthquake and its main aftershocks from teleseismic and strong-motion data. *Geophysical Journal International*, *182*(3), 1411–1430. <https://doi.org/10.1111/j.1365-246X.2010.04685.x>

- Porritt, R. W., Allen, R. M., Boyarko, D. C., & Brudzinski, M. R. (2011). Investigation of Cascadia segmentation with ambient noise tomography. *Earth and Planetary Science Letters*, 309(1-2), 67–76. <https://doi.org/10.1016/j.epsl.2011.06.026>
- Porritt, R. W., Miller, M. S., O'Driscoll, L. J., Harris, C. W., Roosmawati, N., & da Costa, L. T. (2016). Continent–arc collision in the Banda Arc imaged by ambient noise tomography. *Earth and Planetary Science Letters*, 449, 246–258. <https://doi.org/10.1016/j.epsl.2016.06.011>
- Roperch, P., Carlotto, V., Ruffet, G., & Fornari, M. (2011). Tectonic rotations and transient deformation south of the Abancay deflection in the Andes of southern Peru. *Tectonics*, 30, TC2010. <https://doi.org/10.1029/2010TC002725>
- Royden, L. H., Burchfiel, B. C., King, R. W., Wang, E., Chen, Z., Shen, F., & Liu, Y. (1997). Surface deformation and lower crustal flow in eastern Tibet. *Science*, 276(5313), 788–790. <https://doi.org/10.1126/science.276.5313.788>
- Ryan, J., Beck, S. L., Zandt, G., Wagner, L., Minaya, E., & Tavera, H. (2016). Central Andean crustal structure from receiver function analysis. *Tectonophysics*, 682, 120–133. <https://doi.org/10.1016/j.tecto.2016.04.048>
- Salisbury, M. J., Jicha, B. R., de Silva, S. L., Singer, B. S., Jiménez, N. C., & Ort, M. H. (2010).  $^{40}\text{Ar}/^{39}\text{Ar}$  chronostratigraphy of Altiplano-Puna volcanic complex ignimbrites reveals the development of a major magmatic province. *Geological Society of America Bulletin*, 123(5-6), 821–840. <https://doi.org/10.1130/B30280.1>
- Schepers, G., van Hinsbergen, D. J. J., Spakman, W., Kosters, M. E., Boschman, L. M., & McQuarrie, N. (2017). South-American plate advance and forced Andean trench retreat as drivers for transient flat subduction episodes. *Nature Communications*, 8, 15249. <https://doi.org/10.1038/ncomms15249>
- Schilling, F. R., Trumbull, R. B., Brasse, H., Haberland, C., Asch, G., Bruhn, D., et al. (2006). Partial melting in the central Andean crust: A review of geophysical, petrophysical, and petrologic evidence. In *The Andes* (pp. 459–474). Berlin: Springer. [https://doi.org/10.1007/978-3-540-48684-8\\_22](https://doi.org/10.1007/978-3-540-48684-8_22)
- Schmidt, M. W., Vielzeuf, D., & Auzanneau, E. (2004). Melting and dissolution of subducting crust at high pressures: The key role of white mica. *Earth and Planetary Science Letters*, 228(1-2), 65–84. <https://doi.org/10.1016/j.epsl.2004.09.020>
- Scripps Institution of Oceanography (1986). IRIS/IDA seismic network. International Federation of Digital Seismograph Networks. Other/Seismic Network. <https://doi.org/10.7914/SN/II>
- Shapiro, N. M., Ritzwoller, M. H., Molnar, P., & Levin, V. (2004). Thinning and flow of Tibetan crust constrained by seismic anisotropy. *Science*, 305(5681), 233–236. <https://doi.org/10.1126/science.1098276>
- Shen, Z. K., Lü, J., Wang, M., & Bürgmann, R. (2005). Contemporary crustal deformation around the southeast borderland of the Tibetan plateau. *Journal of Geophysical Research*, 110, B11409. <https://doi.org/10.1029/2004JB003421>
- Shirzad, T., & Shomali, Z. H. (2014). Shallow crustal radial anisotropy beneath the Tehran basin of Iran from seismic ambient noise tomography. *Physics of the Earth and Planetary Interiors*, 231, 16–29. <https://doi.org/10.1016/j.pepi.2014.04.001>
- Shirzad, T., Shomali, Z. H., Riahi, M. A., & Jarrahi, M. (2017). Near surface radial anisotropy in the Rigan area/SE Iran. *Tectonophysics*, 694, 414–423. <https://doi.org/10.1016/j.tecto.2016.11.026>
- Silver, P., Beck, S. L., & Wallace, T. (1994). Broadband study of the Altiplano and Central Andes. International Federation of Digital Seismograph Networks. Other/Seismic Network. [https://doi.org/10.7914/SN/XE\\_1994](https://doi.org/10.7914/SN/XE_1994)
- Takeuchi, H., Hamano, Y., & Hasegawa, Y. (1968). Rayleigh- and love-wave discrepancy and the existence of magma pockets in the upper mantle. *Journal of Geophysical Research*, 73(10), 3349–3350. <https://doi.org/10.1029/JB073i010p03349>
- Tassara, A. (2005). Interaction between the Nazca and South American plates and formation of the Altiplano–Puna plateau: Review of a flexural analysis along the Andean margin (15–34°S). *Tectonophysics*, 399(1-4), 39–57. <https://doi.org/10.1016/j.tecto.2004.12.014>
- Tassara, A., & Echaurren, A. (2012). Anatomy of the Andean subduction zone: Three-dimensional density model upgraded and compared against global-scale models. *Geophysical Journal International*, 189(1), 161–168. <https://doi.org/10.1111/j.1365-246X.2012.05397.x>
- Tatham, D. J., Lloyd, G. E., Butler, R. W. H., & Casey, M. (2008). Amphibole and lower crustal seismic properties. *Earth and Planetary Science Letters*, 267(1–2), 118–128. <https://doi.org/10.1016/j.epsl.2007.11.042>
- Turienzo, M., Dimieri, L., Frisicale, C., Araujo, V., & Sánchez, N. (2012). Cenozoic structural evolution of the Argentinean Andes at 34°40'S: A close relationship between thick and thin-skinned deformation. *Andean Geology*, 39(2), 317–357. <https://doi.org/10.5027/andgeoV39n2-a07>
- Universidad de Chile (2013). Red Sismologica Nacional. International Federation of Digital Seismograph Networks. Other/Seismic Network. <https://doi.org/10.7914/SN/C1>
- Wagner, L. S., Beck, L., & Long, M. D. (2010). PerU lithosphere and slab experiment. International Federation of Digital Seismograph Networks. Other/Seismic Network. [https://doi.org/10.7914/SN/ZD\\_2010](https://doi.org/10.7914/SN/ZD_2010)
- Wang, E., & Burchfiel, B. C. (2000). Late Cenozoic to Holocene deformation in southwestern Sichuan and adjacent Yunnan, China, and its role in formation of the southeastern part of the Tibetan plateau. *Geological Society of America Bulletin*, 112(3), 413–423. [https://doi.org/10.1130/0016-7606\(2000\)112%3C413:LCTHDI%3E2.0.CO;2](https://doi.org/10.1130/0016-7606(2000)112%3C413:LCTHDI%3E2.0.CO;2)
- Ward, D., Mahan, K., & Schulte-Pelkum, V. (2012). Roles of quartz and mica in seismic anisotropy of mylonites. *Geophysical Journal International*, 190(2), 1123–1134. <https://doi.org/10.1111/j.1365-246X.2012.05528.x>
- Ward, K. M., Porter, R. C., Zandt, G., Beck, S. L., Wagner, L. S., Minaya, E., & Tavera, H. (2013). Ambient noise tomography across the Central Andes. *Geophysical Journal International*, 194(3), 1559–1573. <https://doi.org/10.1093/gji/ggt166>
- Ward, K. M., Zandt, G., Beck, S. L., Christensen, D. H., & McFarlin, H. (2014). Seismic imaging of the magmatic underpinnings beneath the Altiplano-Puna volcanic complex from the joint inversion of surface wave dispersion and receiver functions. *Earth and Planetary Science Letters*, 404, 43–53. <https://doi.org/10.1016/j.epsl.2014.07.022>
- Wessel, P., & Smith, W. H. F. (1991). Free software helps map and display data. *Eos, Transactions of the American Geophysical Union*, 72(41), 441–446. <https://doi.org/10.1029/90EO00319>
- West, M., & Christensen, D. (2010). Investigating the relationship between pluton growth and volcanism at two active intrusions in the Central Andes. International Federation of Digital Seismograph Networks. Other/Seismic Network. [https://doi.org/10.7914/SN/XP\\_2010](https://doi.org/10.7914/SN/XP_2010)
- Xie, J., Ritzwoller, M. H., Shen, W., Yang, Y., Zheng, Y., & Zhou, L. (2013). Crustal radial anisotropy across eastern Tibet and the western Yangtze craton. *Journal of Geophysical Research: Solid Earth*, 118, 4226–4252. <https://doi.org/10.1002/jgrb.50296>
- Yang, Y., Liu, M., & Stein, S. (2003). A 3-D geodynamic model of lateral crustal flow during Andean mountain building. *Geophysical Research Letters*, 30(21), 2093. <https://doi.org/10.1029/2003GL018308>
- Yuan, X., Sobolev, S. V., Kind, R., & Oncken, O. (2000). Subduction and collision processes in the Central Andes constrained by converted seismic phases. *Nature*, 408(6815), 958–961. <https://doi.org/10.1038/35050073>
- Zandt, G., Leidig, M., Chmielowski, J., Baumont, D., & Yuan, X. (2003). Seismic detection and characterization of the Altiplano-Puna magma body, Central Andes. In *Seismic motion, lithospheric structures, earthquake and volcanic sources: The Keiiti Aki volume* (pp. 789–807). Basel: Birkhäuser. [https://doi.org/10.1007/978-3-0348-8010-7\\_14](https://doi.org/10.1007/978-3-0348-8010-7_14)